High Resolution Synthetic Aperture Radar

Pierfrancesco Lombardo
Department of Information Engineering, Electronic and Telecommunications (DIET)
University of Rome "La Sapienza"Via Eudossiana 18, 00184 – Rome
ITALY

lombardo@infocom.uniroma1.it

ABSTRACT

This manuscript first introduces the fundamentals of Synthetic Aperture radar (SAR), there including the principle of the high resolution imaging capability, the processing required to focus the images, with its constraints and the different acquisition modes. Thereafter, it shows the potential ways to increase the imaging capabilities based on the concept of distributed SAR. Specifically both multistatic and MIMO SAR are considered with both aims of increasing azimuth resolution and increasing the ground range swath.

The formation of increased high resolution images by exploiting the distributed SAR concept is then described in details for a specific application: to increase the cross range resolution of ISAR images of rotating targets. This distributed ISAR technique is devised for two different cases: (i) MIMO case with each platform carrying an active radar, that transmits and receives RF waveforms, (ii) multistatic case with a single platform carrying an active radar (i.e. transmitting and receiving) and the remaining platforms equipped with passive sensors (i.e. receiving only).

The processing chain required to focus the High Resolution distributed ISAR is shown, together with the results obtained against simulated ISAR data for both the MIMO and the multistatic cases. The performance analysis shows that the distributed approach is able to provide an increase of the cross range resolution up to the number of platforms in the multistatic case and even higher in the MIMO case, if the platforms are properly located. This is of great benefit in applications where the target rotation angle is insufficient to guarantee the desired resolution. A typical case is the imaging of ship targets with rotation induced by the sea swell structure under low sea state conditions.

1.0 INTRODUCTION

Nowadays many SAR systems are in operation from both airborne and spaceborne platforms to provide High Resolution radar images. The fundamentals of the SAR image formation are introduced in Section 2, together with the main processing steps required to focus a High Resolution SAR image. Also the main constraints are described for the imaging capabilities of the SAR, together with the different possible acquisition modes, that make a modern SAR flexible to the specific monitoring, intelligence, recognition, or tracking application. Section 2 is also a starting point for material of section 3, where the distributed SAR concept is described. In particular, it is shown that the echoes collected by multiple coherent platforms can be combined to provide increased imaging capabilities, in terms of higher resolution or wider imaged areas.

The specific case of the ISAR (Inverse Synthetic Aperture Radar) is considered to show in greater details the distributed SAR operation. This technique exploits the rotational motion of a target with respect to its

centre, as observed by a nearly stationary sensor platform to provide high resolution images of the target itself, [1]. This is the case of airborne or spaceborne systems (hovering helicopters/UAV or geostationary satellites) imaging ship targets interested by yaw, pitch and roll rotation motions induced by the sea.

Since the achievable cross range resolution depends on the intrinsic motion characteristics of the target (and specifically on its overall change of aspect angle), there is no way to a-priori assign the desired value of cross range resolution, [1], [2]. Moreover, depending on the particular conditions, the achievable resolution can be very poor. For the case of ship targets imaging, this condition can occur in presence of a low sea state inducing very limited rotations: in this case the limited rotation motion can result in a very low cross range resolution. The typical use of the short Coherent Processing Interval that is required by the constraint of keeping fixed the ship rotation axis makes the problem even worse, which degrades the quality of the ISAR images that are often used to feed Non Cooperative Target Recognition procedures, [3]. To increase the cross-range resolution of such ISAR images the distributed ISAR scheme exploits the data acquired by multiple radar sensors carried by multiple air platforms. If the sensors are appropriately spaced, each scatterer can be globally observed from a much wider observation angle than using a single radar and therefore an ISAR image with a higher resolution can be obtained, [4].

Two study cases are considered, consisting of two formations with two and four flying platforms respectively. In the first case study, two sensors are able to observe all the scatterers of the imaged target from two different ranges of viewing angles. An increase in cross-range resolution with respect to the single sensor ISAR case of a factor two is obtained in the bistatic (distributed) ISAR case, while an increase up to a factor three is obtained in the MIMO case. In the second case study with four flying platforms, we achieve a cross-range resolution improvement up to a factor four in the multistatic case and up to a factor nine in the MIMO case.

2.0 SAR FUNDAMENTALS

In the following subsection the principle of SAR is described . Also a short introduction is presented of the techniques used to process the acquired data to focus the high resolution images. The constraints available for the SAR imaging are also introduced together with the different acquisition modes.

2.1 Principle of SAR image formation

The principle of Synthetic Aperture Radar (SAR) image formation is briefly introduced below. We consider a radar carried on a platform flying with velocity V at constant height H. Despite the flat-Earth model is used, typical of airborne SAR geometry, the same concepts apply to the spaceborne SAR geometry. With reference to Fig. 1, we assume that the radar antenna has a rectangular aperture of size $d_a \times d_e$ (azimuth × elevation), with azimuth direction aligned with the velocity vector and elevation direction steered at an angle α_0 from the x-y plane, namely its pointing is steered at an angle α_0 away from the nadir. As apparent, the antenna beamwidth in azimuth and elevation is given respectively by $\psi_a = \lambda / d_a$ and $\psi_e = \lambda / d_e$. Moreover, the area illuminated by the radar pulses is given by the antenna footprint on ground, approximately with size $D_a = \psi_a R_0 = \lambda R_0 / d_a$ in azimuth, being $R_0 = H / \cos\alpha_0$ and $D_e = \psi_e R_0 / \cos\alpha_0 = \lambda R_0 / (d_e \cos\alpha_0)$.

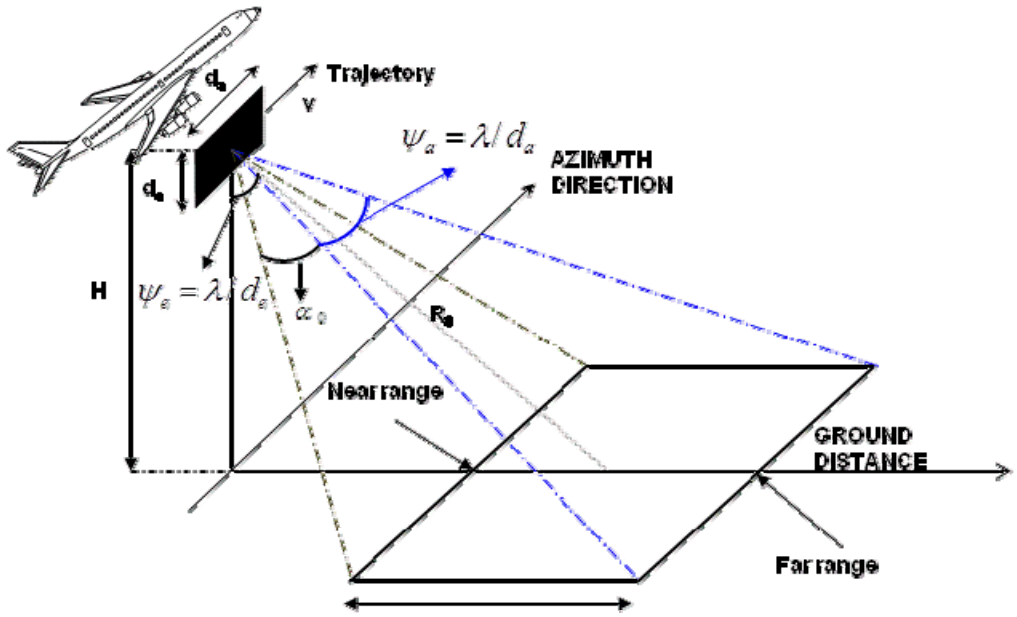

Fig. 1 – Typical airborne SAR geometry.

By transmitting radar waveforms with global frequency bandwidth B, a range resolution of c/2B is available, which allows to resolve narrow strips on ground parallel to the direction of motion. As apparent from Fig. 2, the ground range resolution is given by $c/(2B\sin\theta)$, where θ is the local incidence angle. This is slightly changing from near to far range and in the flat Earth geometry is equal to α_0 at the mid-range point.

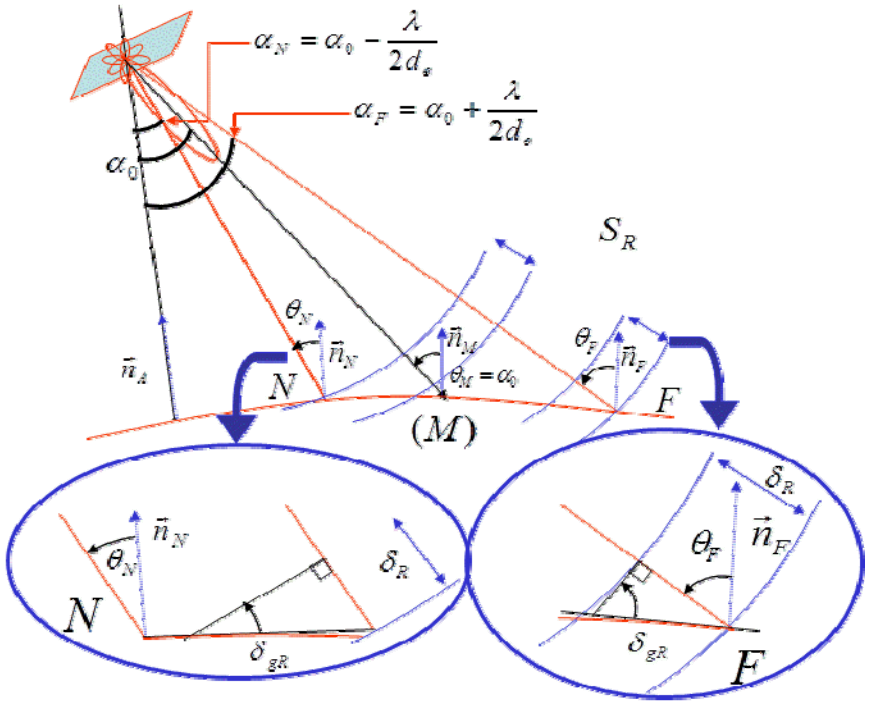

Fig. 2 – SAR ground range resolution.

The narrow strips achieved by each transmitted pulse are depicted in Fig. 3a, which shows the typical operation of a Real Aperture Radar. This is characterized by a high range resolution (that can be set as desired by simply selecting the frequency bandwidth of the transmitted radar waveform, and by a very poor along-track (azimuth) resolution. It is assumed that the radar pulses are transmitted with a constant pulse repetition frequency (PRF) and received back while the platform moves along its trajectory. This pulse-to-pulse time is usually addressed as slow-time, in contrast with the fast-time that characterizes the single pulse traveling in the range direction.

However, Fig. 3b, shows that while the radar moves along its track, the echo back-scattered by the individual object on ground is first received with a high Doppler frequency (i.e. the object is perceived as fast approaching); then its Doppler frequency decreases, till the point where the line of sight radar-object is orthogonal to the velocity (Zero Doppler = zero radial velocity); after that point the object echo is received by the radar with a negative Doppler frequency. This time-varying Doppler frequency is depicted in Fig. 4, that shows clearly that a chirp signal is obtained along the azimuth (slow-time) direction (named t_a). The central frequency f_c is zero in our case, where the antenna is steered orthogonal to the velocity vector, but an azimuth antenna squint $\Delta\varphi$, moves the whole frequency spectrum around $f_c = 2V/\lambda \sin\Delta\varphi$.

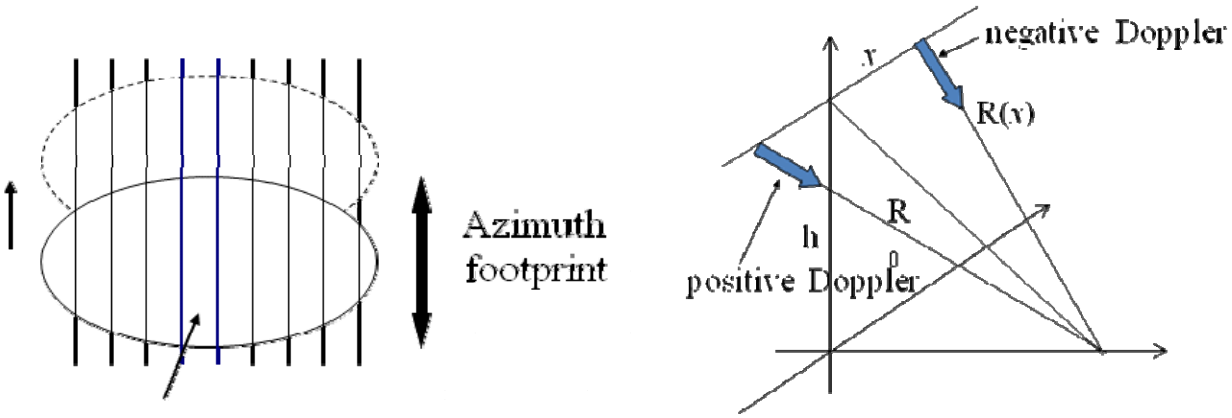

(a) (b)

Fig. 3 – Azimuth returns: (a) Real aperture radar geometry, (b) Doppler frequency change.

This chirp signal is produced by the geometry of the acquisition since, while the radar moves on its trajectory, the radar-to-target distance first reduces and then increases again:

$$R(t_a) = \sqrt{R_0^2 + (V_a \cdot t_a)^2} \cong R_0 + \frac{1}{2R_0} V^2 \cdot t_a^2 \qquad \textbf{(1)}$$

Recalling that the echo signal phase is given by $4\pi R(t_a)/\lambda$, following eq. (1), it has an induced quadratic term. Therefore, its derivative, the Doppler frequency is linear with slow time t_a. Fig. 5 shows that for our geometry the maximum and minimum values of the radial velocity are obtained when the target enters and exits the beam and have modulus $V \sin(\lambda/2d_a)$ that approximates nicely to $V\lambda/2d_a$, due to the small antenna beam aperture. In consequence, the global Doppler frequency bandwidth is $B_{dAZ} = 2V/d_a$. By applying a matched filter in the slow-time domain, it is possible to

compress the azimuth chirp signal. The corresponding resolution is equal to the inverse of the frequency bandwidth in the slow time domain, i.e. $d_a / 2V$, and by scaling this by the platform velocity V, it provides a resolution equal to $d_a / 2$ in the azimuth dimension. This yields the desired high resolution also along the azimuth domain. This can be set as desired by selecting the physical size of the antenna in the azimuth direction, i.e. using a small antenna it is possible to obtain a high azimuth resolution.

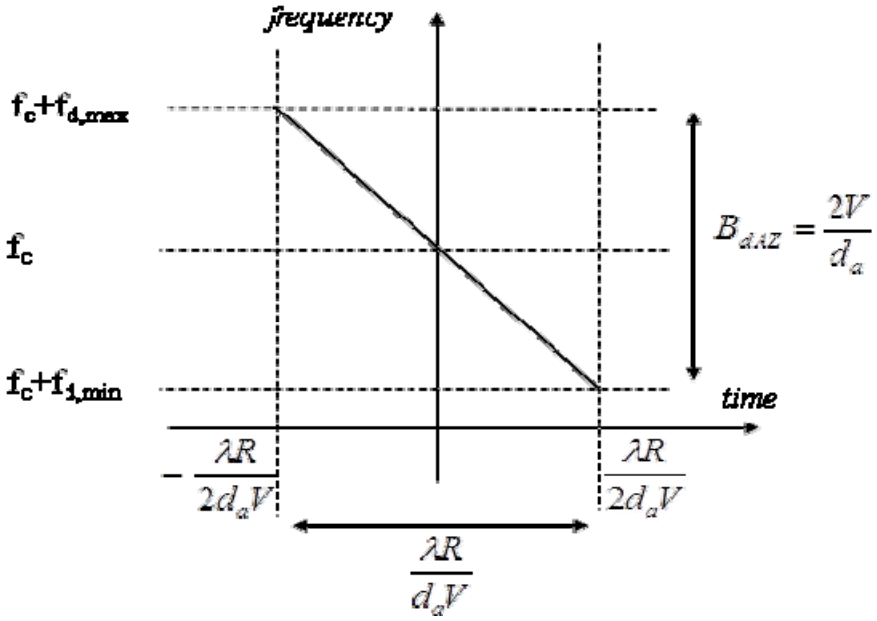

Fig. 4 – Sketch of the Azimuth Chirp waveform.

It can be shown that the application of the matched filter to the azimuth chirp signal is equivalent to the focusing of a synthetic antenna with length corresponding to the whole path flown from the point where the target entered the antenna beam, to the point that it exit the beam, after compensating the quadratic (Fresnel) phase terms of the large synthetic aperture. This explain the name Synthetic Aperture Radar.

As apparent, the high resolution SAR image is obtained by applying matched filtering both along the range and along the azimuth domain, so that a full two-dimensional (2D) processing is required. For high resolution images, the application of the compression filter along the two dimensions is not separable for two reasons:

(i) due to the variation of the radar-to-target distance during the platform motion, the radar echoes might not be only phase shifted, but they can be readily received in different range resolution cells, for a given flight geometry. This effect is obviously stronger when the range resolution cell is smaller (higher resolution). This phenomenon, that goes under the name of Range Cell Migration (RCM) needs to be compensated before it is possible to apply a matched filter in the azimuth domain.

(ii) the azimuth quadratic phase term in eq. (1) has been derived for the central point inside the antenna footprint and it depends on the inverse of R_0. However, for points on ground at different ranges, R_0 must be replaced with the actual minimum distance from the radar. This means that the azimuth matched filter changes with range. In a similar way also the RCM compensation must be modified as a function of range.

Globally, the focusing of a high resolution SAR image requires a 2D spatially variant filtering procedure. While it is possible to implement this filtering in the fast-time /slow-time bidimensional domain, it certainly requires a high cost. Different techniques are available to apply this filtering with a limited computational

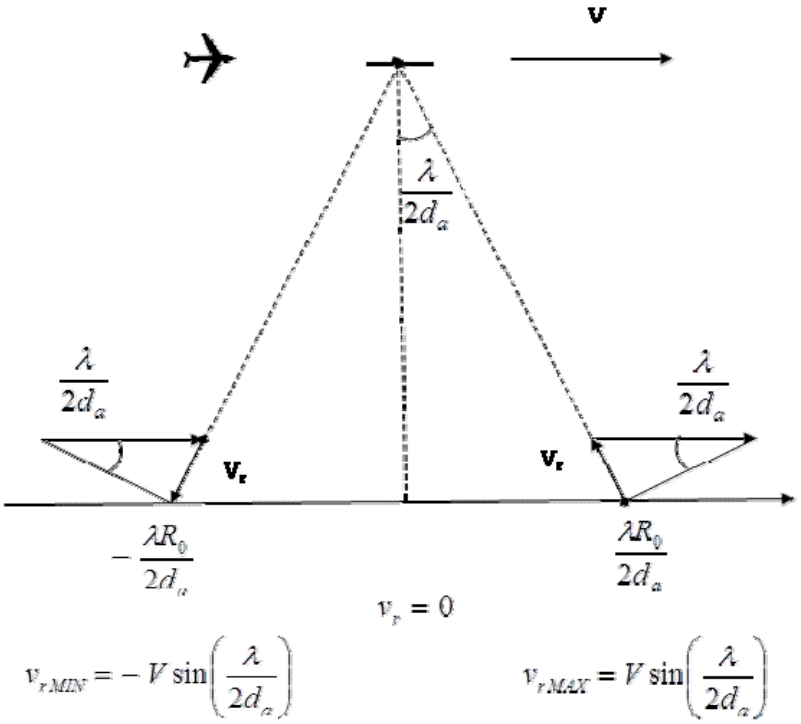

Fig. 5 – Radial velocity along the radar path.

load that can exploit one or more frequency domains (see Fig. 6). In particular, the Chirp Scaling Algorithm (CSA), splits the global filtering and RCM compensation procedure in different steps to be applied in different time or Doppler Domains. In particular, it exploits the Chirp signal properties to obtain that the full processing is reduced to a sequence of Fast Fourier Transforms (FFT) and products by phase factors, [5]. As depicted in Fig. 7: (i) the first operation is an azimuth FFT, followed by a phase product that equalizes the RCM curvature (from near to far range) in this fast-time / azimuth Doppler domain; (ii) a range FFT moves

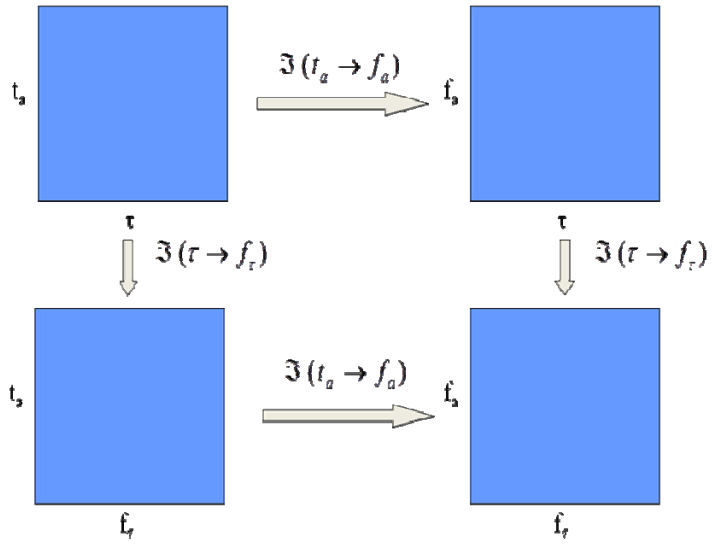

Fig. 6 – The four domains for the application of the 2D SAR focusing.

the data in the range Doppler/ azimuth Doppler domain, where the RCM is compensated and the range compression is performed; (iii) an Inverse range FFT brings back into the fast-time / azimuth Doppler domain, where the azimuth compression is applied and the remaining spurious terms are compensated; and (iv) the final azimuth Inverse FFT provides the focused image in the desired range azimuth domain.

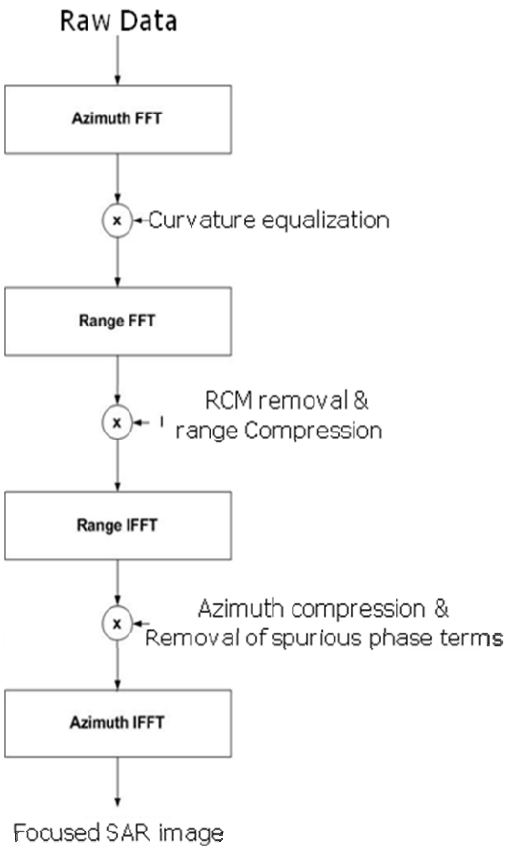

Fig. 7 – Sketch of the Chirp Scaling Algorithm.

2.2 SAR fundamental limitation and acquisition modes

As stated in the previous section, the maximum azimuth resolution of $d_a/2$ can be obtained using all the echoes backscattered by the target when illuminated by the antenna beam. As apparent from Fig. 8, this corresponds to a whole synthetic aperture D_s equal to the antenna footprint. Moreover, the obtained azimuth resolution can be justified using the standard equation $\lambda/(2\Delta\theta)$ being $\Delta\theta$ the observation angle by which the point scatterer is observed. From Fig. 8, $\Delta\theta = \phi_a = \lambda / d_a$ so that the final resolution is equal to $d_a/2$.

We also notice that if the antenna pointing is maintained fixed at 90° with respect to the velocity vector, it is impossible to further increase the observation angle and therefore to further improve the azimuth resolution. However, the same resolution can be achieved for all the points along a very long (possibly infinity) strip in azimuth, so that this acquisition geometry is known as STRIPMAP SAR.

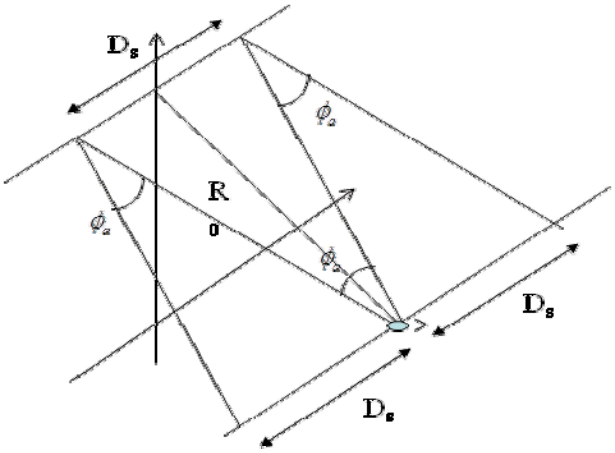

Fig. 8 – STRIPMAP SAR geometry.

It is interesting to observe that SAR acquisition is subject to two constraints: the PRF must be greater than the Doppler frequency bandwidth seen by the moving antenna (to avoid azimuth frequency ambiguities as from the Nyquist Sampling Theorem):

$$PRF \geq 2V / d_a \tag{2}$$

In addition, to avoid range ambiguities its inverse must be greater than the time required for all echoes from the whole antenna footprint to be received. This quantity is obtained by converting in time the slant range swath S_R, which is approximately obtained by projection the antenna footprint in ground range on the line of sight: $S_R = D_e \sin \alpha_0$.

$$1/PRF \geq 2S_R / c = 2\psi_e R_o / \cos \alpha_0 = \lambda / d_e R_o / \cos \alpha_0 \tag{3}$$

Therefore the PRF must be selected between a lower and a upper bound:

$$\frac{2v}{\lambda}\frac{\lambda}{d_a} \leq PRF \leq \frac{c}{2}\frac{d_e \cos \alpha_0}{\lambda R_o} \tag{4}$$

For this to be applicable, it is required that the inequality applies between lower and upper bound. This inequality can be rewritten in two different ways:

$$\frac{D_e}{d_a/2} \leq \frac{c}{2v \sin \alpha_0} \tag{5}$$

$$d_e d_a \geq \frac{4v}{c}\frac{\lambda R_o}{\cos \alpha} \tag{6}$$

The former expression states that the ratio between size of the imaged area in range and azimuth resolution cannot exceed a fixed quantity, which is determined by platform velocity and off-nadir angle. Namely, it is not possible to obtain an image of a very large strip of ground at a very high resolution: high resolution can only be achieved for small areas, whereas large areas can only be imaged at lower resolution. This sets a constraint on the amount of information present in a STRIPMAP SAR image.

The latter expression states that the antenna area must be larger than a quantity only related to the geometry. It is clearly directly related to the first expression, and has implications on the system design.

Once the antenna has been designed for the STRIPMAP acquisition, it is possible to image wider areas, by scanning the antenna beam in elevation to cover multiple strips on ground. The switching among the set of elevations must be made inside a time shorter than the time required to the platform to cover the whole maximum synthetic aperture D_a. This allows to avoid gaps in the imaged area (see Fig. 9), but it results in a reduced effective observation angle $\Delta\theta = \phi_a / N_{scan}$ equal to a fraction (about 1/number of scanned elevation angles) of the original full STRIPMAP angle $\Delta\theta = \phi_a$, therefore the azimuth resolution decreases by a factor N_{scan}. This is fully consistent with the constraint in eq. (5) and is known as ScanSAR.

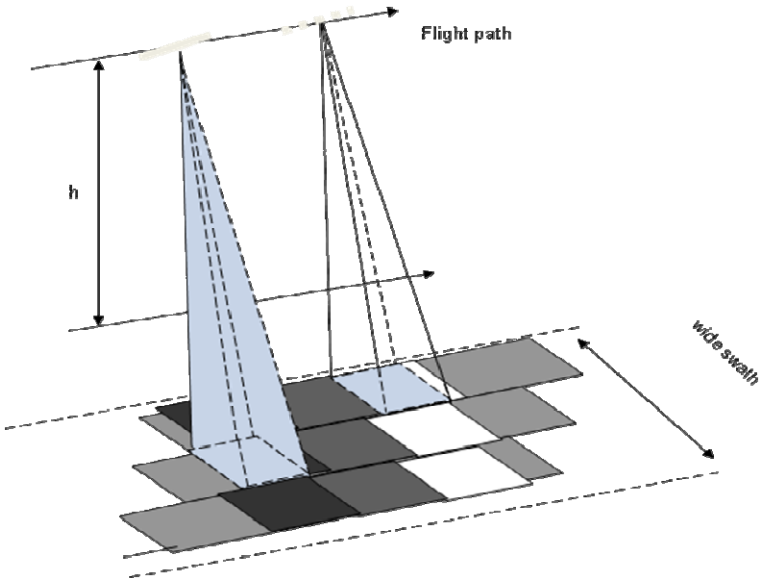

Fig. 9 – ScanSAR geometry.

The possibility to obtain a higher resolution than allowed from eq. (5) for an assigned range swath size is often of great interest to detect, identify and track specific targets. A possibility is to modify the antenna steering during the SAR acquisition time, acting as a spotlight: the antenna beam is steered in azimuth toward a specific point on ground, which is the centre of the area to be imaged (see Fig. 10b). In this way, the echoes from the individual point on ground start earlier to be received by the radar and ends later than in the STRIPMAP mode (Fig. 10a). The increased observation time provides higher maximum and minimum Doppler frequencies and therefore a wider azimuth frequency bandwidth, which in turn yields a higher resolution after azimuth compression. This acquisition mode is known under the name of Spotlight SAR.

It is interesting to observe that the increased resolution can also be explained by resorting to the change in the effective observation angle: in the Spotlight SAR mode, the effective observation angle for the points on ground inside the antenna footprint is increased, thus providing higher resolution.

It is interesting to observe that violating the STRIPMAP constraint in eq. (5) is paid by the neat reduction of the imaged area in the azimuth domain. By steering the antenna toward a specific area, only this small azimuth area (about the antenna footprint) can be imaged at high resolution, and the continuous strip is not available any more. For the sake of simplicity, we notice that it is also possible a hybrid STRIP/spot mode, where the antenna is steered with some inertia toward the centre, so to provide a compromise solution with a wider azimuth area than Spotlight SAR and azimuth resolution in between STRIP and Spot modes.

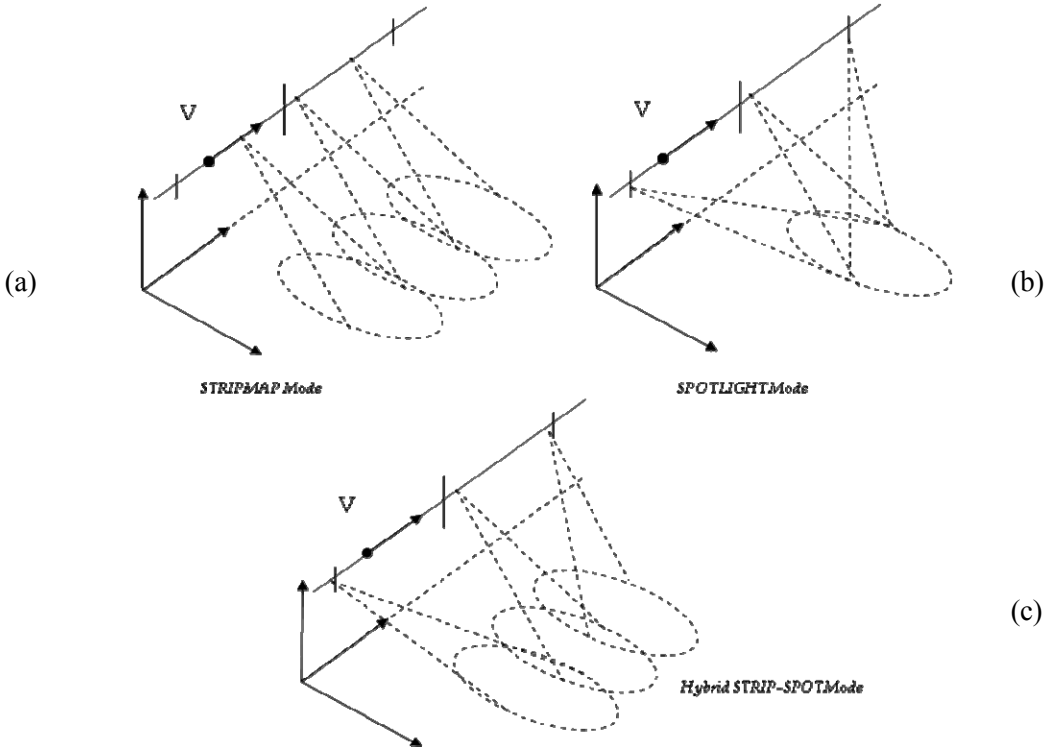

Fig. 10 - Comparison of SAR acquisition modes: (a) STRIPMAP, (b) Spotlight SAR, (c) Hybrid STRIP/Spot.

Finally, we notice that the important element is not the motion of the radar platform, but the relative motion between radar and point to be imaged. In facts, essentially the same signals would be received if the radar was in a fixed position and the target rotates in a way to show an effective change of observation angle $\Delta\theta$. This is the acquisition mode known as Inverse SAR (ISAR), that allows to image moving vehicles with stationary radar, as for example flying aircrafts, sailing ships, or non-sailing ship targets rotating by the effect of the sea waves.

3.0 DISTRIBUTED SAR/ISAR

The distributed SAR concept can be used to increase the imaging capability using multiple platforms. For example, if three STRIPMAP SAR platforms are used, as in Fig. 11a, and leading and trailing platforms use antenna beams appropriately squinted in azimuth respectively backwards and forwards, it is clearly possible to recombine the echoes received from the three platforms to emulate an effective observation angle three times larger. Therefore, a distributed STRIPMAP SAR could provide an azimuth resolution three times better than a standard STRIPMAP SAR, without losing the continuity of the imaged strip.

While a Spotlight SAR typically does not need a distributed system, the use of multiple platforms allows to reduce the global acquisition time, as clear from the sketch of Fig. 11b, where each of the three platforms collects echoes simultaneously from one third of the full trajectory. This can be of interest, when it is highly important to reduce the acquisition time, because of the hostile environment.

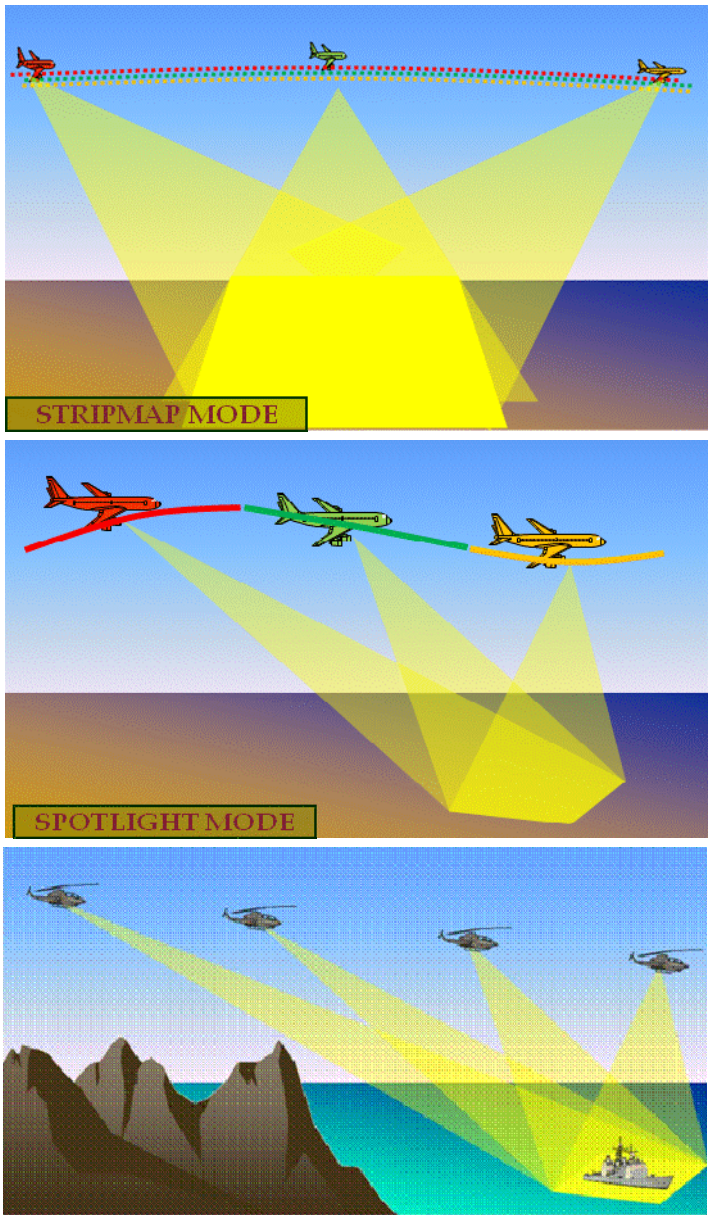

(a)

(b)

(c)

Fig. 11 – Distributed SAR concept for increased resolution: (a) STRIPMAP, (b) Spotlight, (c) ISAR.

The ISAR case is shown in Fig. 11c, where each platform observes a fraction of the target rotation. This can be of high interest to obtain high resolution ISAR images of stationary ships, when the sea-induced rotations are too limited to provide a global high resolution image and is detailed in the following sections.

In general, the use of N sensors provides an improvement of a factor N. This can be in terms of resolution, as illustrated in Fig. 11, but it could also be used to relax the PRF constraint, namely to increase the range swath. For example, Fig. 12a shows the used of three STRIPMAP SAR platforms, where each one uses a PRF three time lower that a standard STRIPMAP SAR. In this way, the each of the platform can take samples from a three time wider swath. The individual sensor operates with azimuth undersampling so that its image is aliased. However, by recombining the samples from the three platforms, an image three times wider in range can be obtained with the full STRIPMAP SAR resolution. Fig. 12b shows that it is not required that the platforms fly very close one another, but they must transmit and receive the waveforms when they reach the appropriate positions along the track.

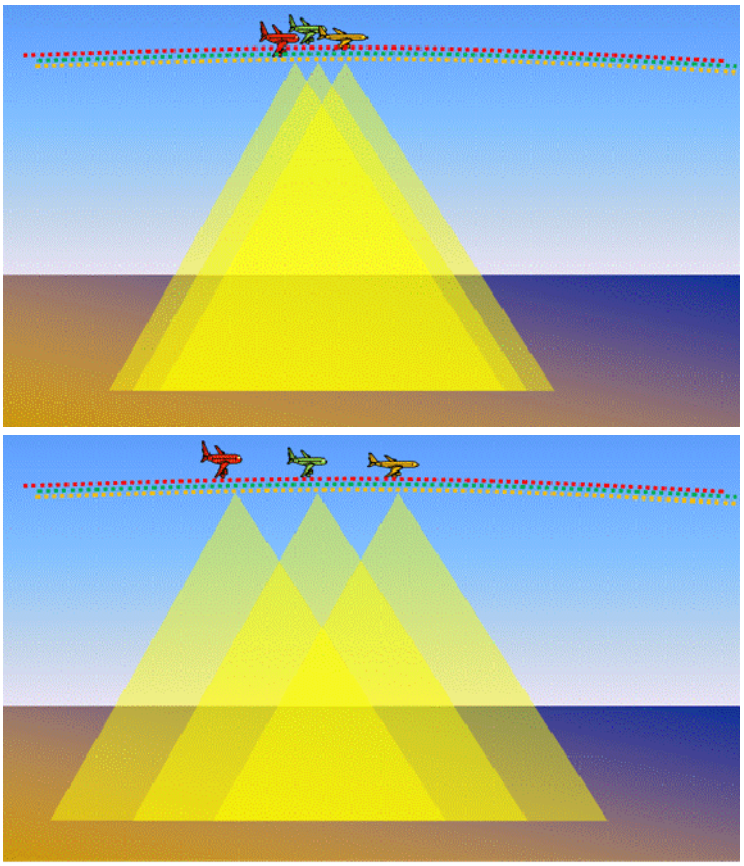

(a)

(b)

Fig. 12 – Distributed STRIPMAP SAR concept for increased range swath: (a) closely, (b) widely separated sensors.

As apparent, for this distributed strategy it is not necessary that each platform transmits its own waveform and it is often enough that one of the platforms has the transmitter on board, while the remaining N-1 have just a receiver. However, all the receivers of such a distributed system with echoes to be coherently combined require a full coherency of the oscillators and possibly appropriate synchronization strategies. Therefore, the advantage of requiring a single transmitter is partially compensated by the requirement of coherency and synchronization.

However, it is interesting to observe that if, in addition to the synchronization, all sensors:

(i) operate at the same time,

(ii) are able to transmit and use orthogonal waveforms,

(iii) are able to receive also the backscattered echoes corresponding to the other transmitters,

a complete MIMO (Multiple Input Multiple Output) SAR system is obtained. In the simple example of two platforms, the possibility that one of the platforms receives the backscattered echoes corresponding to the transmissions of the other, provides an observation position (namely a virtual platform) that is exactly midway between the two real platforms (see Fig. 13). This is equivalent to the presence of three equispaced platforms.

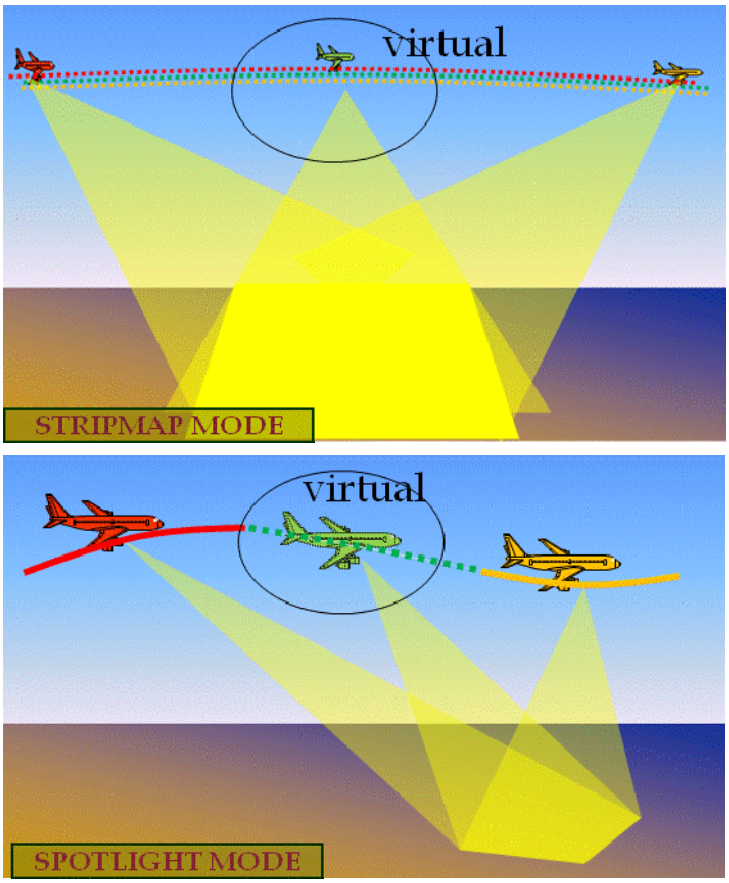

Fig. 13 – MIMO virtual platform with distributed SAR: (a) STRIPMAP, (b) Spotlight.

Generally, using the MIMO SAR approach, with S real sensors, it is possible to obtain an improvement either in resolution or in range swath greater than S, which depends on the specific platforms positions.

For the interested reader, it is noticed that the use of multiple sensors for SAR application has been studied in various contributions in the literature. The exploitation of the multiple sensors aiming at removing (or reducing) range and/or azimuth ambiguities was shown to allow overcoming the fundamental ambiguity limitation of monostatic SAR, especially when working in the STRIPMAP configuration, for which the azimuth resolution poses contradicting system requirements with the unambiguous swath width [6], [7], [8]. The case of STRIPMAP SAR having to deal with the fundamental ambiguity limitation is typically the most demanding one, since in the spotlight SAR case (also addressed by [9],[10]) the increase of cross-range resolution is typically easily achieved with a single platform by using a longer acquisition time. Moreover, the possibility to use the MIMO approach to increase the SAR range resolution was introduced in [11], using a cross-range alignment of sensors.

In the ISAR case the resolution depends on the intrinsic target motion, and often it is not possible to increase the resolution by extending the acquisition time. Therefore, the exploitation of multiple sensors by means of the proposed distributed ISAR approach is the enabling solution to achieve the ISAR images with desired resolution, and finally the desired NCTR performance.

To illustrate in details this potentiality, in the following subsection the distributed ISAR observation geometry is introduced, and the improvements available for both multistatic and MIMO cases is shown,

with respect to the single sensor ISAR. As apparent similar results could be described for the other SAR acquisition modes.

Again for the interested reader, it is noted that multiple sensors have been considered for ISAR imaging, but their use has been only to add interferometric capability, [12], [13]. However, in [4],[17],[18] the multiple sensors have been exploited to increase the cross-range resolution.

To show this case in details, the bistatic ISAR geometry and resolution are introduced in section 3.1 and then the distributed ISAR is shown in section 3.2. The considered distributed ISAR geometry consists essentially of a set of S air-platforms, each one with equipped with a sensor, characterized by either: (i) transmitting, or (ii) receiving, (iii) or both transmitting and receiving capability. All sensors are assumed to carry an antenna appropriately steered toward the moving target to be imaged, by exploiting its own rotational motion. Moreover, for the sake of simplicity the platforms are considered stationary, as for example hovering helicopters or balloons, or other similar unmanned platforms.

3.1 Bistatic ISAR Geometry and resolution

As usual in ISAR literature, an arbitrary reference point in the target, called target fulcrum is selected, and the target motion is decomposed into a translation of the fulcrum (which is assumed to be already compensated for) and a rotation of the target body around this point (rigid body hypothesis). The interest is in targets with a dominant rotation around the vertical axis (resulting in a plane image [2]), therefore pitch and roll are considered negligible w.r.t. the yaw component of the motion. The origin of the coordinate reference system is set in the target fulcrum (see Fig. 14) and the target is assumed to rotate with a rate ω around the Z axis.

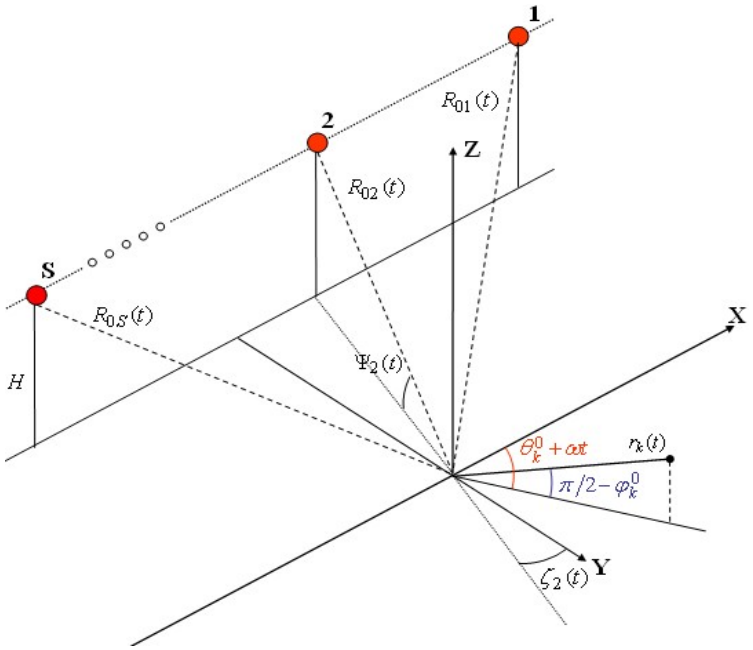

Fig. 14 – Acquisition geometry description.

The distributed target (for example a ship) is modelled as a rigid body consisting of a set of K scatterers with position vectors $\mathbf{r}_k(t) = r_k \cdot \hat{\mathbf{r}}_k(t)$, k=1, ..., K, where the vector length $r_k = \|\mathbf{r}_k(t)\|$ and the elevation angle ϕ_k are constant, while the unit vector $\hat{\mathbf{r}}_k(t)$ is characterized by a rotation around the Z axis with constant angular velocity ω and initial azimuth angle θ_k^0 measured in clockwise direction from X (i.e. $\theta_k(t) = \theta_k(0) + \omega t = \theta_k^0 + \omega t$), namely:

$$\mathbf{r}_k(t) = \begin{bmatrix} r_k \sin\phi_k \cos(\theta_k^0 + \omega t) \\ r_k \sin\phi_k \sin(\theta_k^0 + \omega t) \\ r_k \cos\phi_k \end{bmatrix} \tag{7}$$

The complex reflectivity of the K scatterers is assumed constant during the observation time T and independent of the observation angle, which is reasonable for small angles of view.

The sketch in Fig. 14 also defines the position vector $\mathbf{R}_{0i}(t)$ of the *i-th* platform, i=1, …, S, that are assumed to be aligned at the same height H and its unit vector $\hat{\mathbf{r}}_{0i}(t) = \mathbf{R}_{0i}(t) / |\mathbf{R}_{0i}(t)|$:

$$\hat{\mathbf{r}}_{0i}(t) = \begin{bmatrix} +\cos(\psi_i(t))\sin(\zeta_i(t)) \\ -\cos(\psi_i(t))\cos(\zeta_i(t)) \\ \sin(\psi_i(t)) \end{bmatrix} \tag{8}$$

where $\psi_i(t)$ is the grazing angle for the *i-th* platform at time *t*, and $\zeta_i(t)$ is the azimuth angle, measured in clockwise direction from Y.

Using the position vectors and definitions above, and assuming that the platform distance is much larger than the target size (namely $|\mathbf{R}_{0i}(t)| >> |\mathbf{r}_k(t)|$ for i=1, ..., S, k=1, ..., K), the distance between the i-th platform and the k-th target scatterer can be written as

$$|\mathbf{R}_{0i}(t) - \mathbf{r}_k(t)| \approx |\mathbf{R}_{0i}(t)| - \hat{\mathbf{r}}_{0i}(t) \cdot \mathbf{r}_k(t) \tag{9}$$

This, in turn implies that the echo reflected from the k-th scatterer when the radar waveform is transmitted by platform *i* and received by platform *j* must propagate at distance equal to

$$|\mathbf{R}_{0i}(t) - \mathbf{r}_k(t)| + |\mathbf{R}_{0j}(t) - \mathbf{r}_k(t)| = 2\left(R_{i,j}(t) - \Delta R_{ij,k}(t)\right) \tag{10}$$

where

$$R_{i,j}(t) = \frac{|\mathbf{R}_{0i}(t)| + |\mathbf{R}_{0j}(t)|}{2} \quad \text{and} \quad \Delta R_{ij,k}(t) = \frac{\left[\hat{\mathbf{r}}_{0i}(t) + \hat{\mathbf{r}}_{0j}(t)\right]}{2} \cdot \mathbf{r}_k(t) \tag{11}$$

Assuming the grazing angle nearly constant for all platforms $\psi_i(t) \approx \psi_0(t)$ i=1,…,S, the sum of the unit vectors becomes:

$$\mathbf{r}_{0i,j}(t) = \frac{\hat{\mathbf{r}}_{0i}(t)+\hat{\mathbf{r}}_{0j}(t)}{2} = \begin{bmatrix} +\cos(\psi_0(t))\ \sin(\alpha_{i,j}(t))\cos(\beta_{i,j}(t)) \\ -\cos(\psi_0(t))\cos(\alpha_{i,j}(t))\cos(\beta_{i,j}(t)) \\ \sin(\psi_0(t)) \end{bmatrix} \quad \textbf{(12)}$$

with mean angle $\alpha_{i,j}(t) = \frac{\zeta_i(t)+\zeta_j(t)}{2}$ and half difference angle $\beta_{i,j}(t) = \frac{\zeta_i(t)-\zeta_j(t)}{2}$. For monostatic acquisitions we have *i=j*, so that $\beta_{i,j}(t) = \beta_{i,i}(t) = 0$ and the mean angle is exactly the azimuth angle of the i-th platform: $\alpha_{i,j}(t) = \alpha_{i,i}(t) = \zeta_i(t)$ so that $\mathbf{r}_{0i,j}(t) = \hat{\mathbf{r}}_{0i}(t)$. In contrast, in the bistatic case (namely $i \neq j$) $\mathbf{r}_{0i,j}(t)$ is not strictly a unit vector. However, assuming that the azimuth angular difference of the different platforms is small, $\beta_{i,j}(t)$ is a small number so that $\cos(\beta_{i,j}(t))$ is close to unity. In this case the bistatic configuration is approximated very closely by a monostatic configuration with unit vector:

$$\hat{\mathbf{r}}_{0i,j}(t) = \begin{bmatrix} +\cos(\psi_0(t))\ \sin(\alpha_{i,j}(t)) \\ -\cos(\psi_0(t))\cos(\alpha_{i,j}(t)) \\ \sin(\psi_0(t)) \end{bmatrix} \quad \textbf{(13)}$$

This corresponds to an equivalent monostatic configuration with a fictitious sensor at azimuth angle $\alpha_n = \alpha_{i,j}(t)$, namely the mean angle between the real transmit and receive platforms. The equivalent position vector of the fictitious sensor is completely characterized by the same elevation angle, $\psi_0(t)$ of the real sensors and an equivalent length equal to $R_n = R_{i,j}(t) = (|\mathbf{R}_{0i}| + |\mathbf{R}_{0j}|)/2$. This equivalence allows us to treat with a unified notation all distributed ISAR configurations: monostatic, bistatic, and MIMO. Assuming that the platforms are exactly stationary, or that their motion components have been estimated and compensated, [14], [15], [16], the phase shift of the received signal for the generic case of using the (transmit, receive) sensors couple (i, j) for the specific observation depends on time only by means of the target rotational motion around the Z axis:

$$\begin{aligned} \Delta\Phi_{i,j}(t) &\cong -j\frac{4\pi}{\lambda}\left[R_{i,j} - \hat{\mathbf{r}}_{0i,j}\cdot\mathbf{r}_k(t)\right] = \\ &= -j\frac{4\pi}{\lambda}\left[R_{i,j} - r_k\cos\varphi_k\sin\psi_0 + r_k\sin\varphi_k\cos\psi_0\sin(\theta_k^0 - \alpha_{i,j} + \omega t)\right] \end{aligned} \quad \textbf{(14)}$$

where only the mean angle $\alpha_n = \alpha_{i,j} = \left[\zeta_i + \zeta_j\right]/2$ determines the phase modulation characteristics, together with the rotation rate ω. The change of aspect angle during time is easily observed to be linear in the slow-time with the same rate for all equivalent sensors, but with different starting angles α_n.

Before introducing the distributed ISAR concept, it is useful to recall the expected performance for the standard ISAR imaging obtained by a single equivalent sensor. We assume that the total ISAR image acquisition time T is limited due to the intrinsic period of the target rotation motion around the Z axis (yaw motion). As recalled in section 2, the cross-range resolution achievable with the ISAR processing is equal to $\Delta cr = \frac{\lambda}{2\Delta\theta}$, being $\Delta\theta$ the global variation of the view angle of observation of the individual point scatterer, [1]-[2]. This angle is the argument of the last sinusoidal component in the phase of eq.

(13). This angle is clearly changing with time with rate ω due to the rotation to the scatterer. Assuming the observation time t spans in [-T/2, T/2], the global variation of the view angle for the generic *r-th* scatterer, for the case of the single *n-th* equivalent sensor, is given by:

$$\Delta\theta = \theta_k^n(t)\Big|_{t=T/2} - \theta_k^n(t)\Big|_{t=-T/2} = \left[\theta_k^0 - \alpha_n + \omega\,(T/2)\right] - \left[\theta_k^0 - \alpha_n + \omega(-T/2)\right] = \omega\,T \qquad \textbf{(15)}$$

Based on eq. (13), the global received signal becomes:

$$s_n(t) = e^{-j\frac{4\pi}{\lambda}\left[R_n - r_k\cos\varphi_k\sin\psi_0 + r_k\sin\varphi_k\cos\psi_0\sin(\theta_k^0 - \alpha_n + \omega t)\cos\beta_n\right]}\, rect_T(t) \qquad \textbf{(16)}$$

For the equivalent sensor *n*, the range axis is aligned with angle α_n, and the cross-range direction is orthogonal to it. Therefore, the scatterer range and cross-range positions are respectively $x_r^{k(n)} = r_k\sin\varphi_k\sin(\theta_k^0 - \alpha_n)$ and $x_{cr}^{k(n)} = r_k\sin\varphi_k\cos(\theta_k^0 - \alpha_n)$, so that assuming a small $\Delta\theta$:

$$s_n(t) \cong e^{-j\frac{4\pi}{\lambda}\left[R_n - r_k\cos\varphi_k\sin\psi_0 + (x_r^{k(n)} - x_{cr}^{k(n)}\omega t)\cos\beta_n\right]}\, rect_T(t) \qquad \textbf{(17)}$$

The cross-range focusing can be approximated by a Fourier Transform evaluated for $f = -\frac{2\omega}{\lambda}\cos\beta_n\, x_{cr}$:

$$I_n(x_{cr}) = S_n(f)\Big|_{f=-\frac{2\omega}{\lambda}\cos\beta_n x_{cr}} =$$

$$\cong e^{-j\frac{4\pi}{\lambda}\left[R_n - r_k\cos\phi_k\sin\psi_0 + x_r^{k(n)}\cos\beta_n\right]}\, T\,\mathrm{sinc}\left[\pi\frac{2\omega}{\lambda}T\cos\beta_n\,(x_{cr} - x_{cr}^{k(n)})\right] \qquad \textbf{(18)}$$

This clearly shows that the scatterer echo is correctly imaged at the position $x_{cr}^{k(n)}$. The cross-range resolution can also be clearly by obtained by the first null of the sinc(x) function to be equal to $\Delta cr_n = \lambda/(2\omega T\cos\beta_n)$.

3.2 Dual Platform ISAR Concept

In the following we introduce the dual platform ISAR concept, as a first step toward distributed ISAR concept with a generic number N of sensors. The idea is to increase the cross-track resolution by exploiting multiple equivalent sensors to increase the global variation of the view angle. Thanks to the equivalent monostatic model, we can define the scenario with direct reference to the equivalent sensors, as depicted in Fig. 15. Reference is made to the case of two adjacent equivalent sensors, i.e. sensor *n* and

sensor *n-1*. While each sensor independently observes the *r-th* scatterer with an angle $\Delta\theta = \omega\, T$, the two observation angles are not totally overlapped, in fact the time varying value of the observation angle experienced by the sensor *n* and *n-1* are given by the following expressions:

$$\theta_k^n(t) = \theta_k^0 - \alpha_n + \omega t \qquad -T/2 \le t \le T/2 \tag{19}$$

$$\theta_k^{n-1}(t) = \theta_k^0 - \alpha_{n-1} + \omega t \qquad -T/2 \le t \le T/2$$

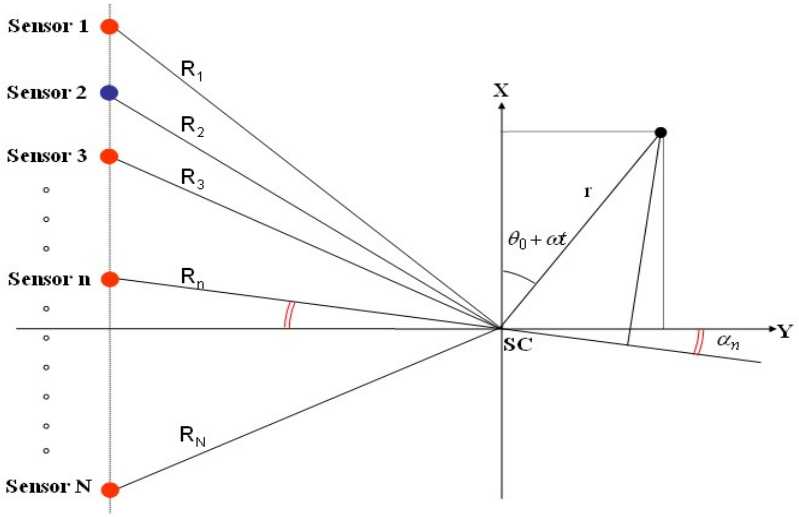

Fig. 15 – Acquisition geometry description using N equivalent sensors.

This is depicted in Fig. 16, from which it is easy to verify that the global change of the view angle for the *k-th* scatterer is given by (recall that from the geometry of Fig. 15 $\alpha_{n-1} \ge \alpha_n$), [4]:

$$\Delta\theta_{eff}^{(n,n-1)} = \theta_k^n(T/2) - \theta_k^{n-1}(-T/2) = \left[\theta_k^0 - \alpha_n + \omega T/2\right] - \left[\theta_k^0 - \alpha_{n-1} - \omega T/2\right] = \omega T + \alpha_{n-1} - \alpha_n \tag{20}$$

The global observation angle in eq. (19), is greater than ωT and can provide increased resolution. In order to avoid gaps in the overall view angle, it is required that $\theta_k^n(-T/2) \le \theta_k^{n-1}(T/2)$, namely: $\alpha_{n-1} - \alpha_n \le \omega T$. Therefore, the effective observation angle with the two equivalent sensors is limited by the inequality: $\Delta\theta \le \Delta\theta_{eff}^{(n,n-1)} \le 2\Delta\theta$ and the cross range resolution becomes

$$\Delta cr = \frac{\lambda}{2\Delta\theta_{eff}^{(n,n-1)}} = \frac{\lambda}{2(\omega T + \alpha_{n-1} - \alpha_n)} \ge \frac{\lambda}{4\Delta\theta} \tag{21}$$

Where the equality applies only for the maximum allowable angle $\alpha_{n-1} - \alpha_n = \omega T = \Delta\theta$.

To obtain the increased cross-range resolution, in principle, the signals received by the two equivalent sensors can be combined as

$$s_{comb}(t)=e^{j\frac{4\pi}{\lambda}R_{n-1}}s_{n-1}(t+t_n')rect_{T_n'}(t+T_n'/2)+e^{j\frac{4\pi}{\lambda}R_n}s_n(t-t_n')rect_{T_n'}(t-T_n'/2) \quad \textbf{(22)}$$

where $T_n' = \frac{T}{2}+\frac{\alpha_{n-1}-\alpha_n}{2\omega}$ and $t_n' = \frac{\alpha_{n-1}-\alpha_n}{2\omega}$. By assuming constant $\beta_{n-1} = \beta_n$ (namely neglecting the bistatic differences), this yields, [4]:

$$s_{comb}(t)=e^{-j\frac{4\pi}{\lambda}\left[-r_k\cos\varphi_k\sin\psi_0+r_k\sin\varphi_k\cos\psi_0\sin(\theta_k^0-\frac{\alpha_{n-1}+\alpha_n}{2}+\omega t)\cos\beta_n\right]}rect_{2T_n'}(t) \quad \textbf{(23)}$$

The global cross-range direction is now defined by angle $(\alpha_{n-1}+\alpha_n)/2$, so that the scatterer range and cross-range positions are respectively $x_r^k = r_k \sin\varphi_k \sin(\theta_k^0-(\alpha_{n-1}+\alpha_n)/2)$ and $x_{cr}^k = r_k \sin\varphi_k \cos(\theta_k^0-(\alpha_{n-1}+\alpha_n)/2)$. By comparing eq. (24) with eq. (14), it is apparent that exactly the same procedure can be applied than in eqs. (16) – (17), thus yielding a correctly positioned scatterer in cross-range with resolution $\Delta cr_n = \lambda/(2\omega 2T_n\cos\beta_n)$. This shows the increased resolution corresponding to an overall angle $\omega T+\alpha_{n-1}-\alpha_n$.

The time-varying observation angle of the multistatic case is sketched in Fig. 16A, for the case where the first sensor is a monostatic (transmit and receive radar) while the second sensor is a receiving-only sensor, positioned so to provide the appropriate change in the view angle (namely $\alpha_{n-1}-\alpha_n$). With the two sensors, the maximum increase achievable in observation angle, and therefore in resolution, is of a factor of 2, which is obtained by setting $\alpha_{n-1}-\alpha_n = \omega T = \Delta\theta$,

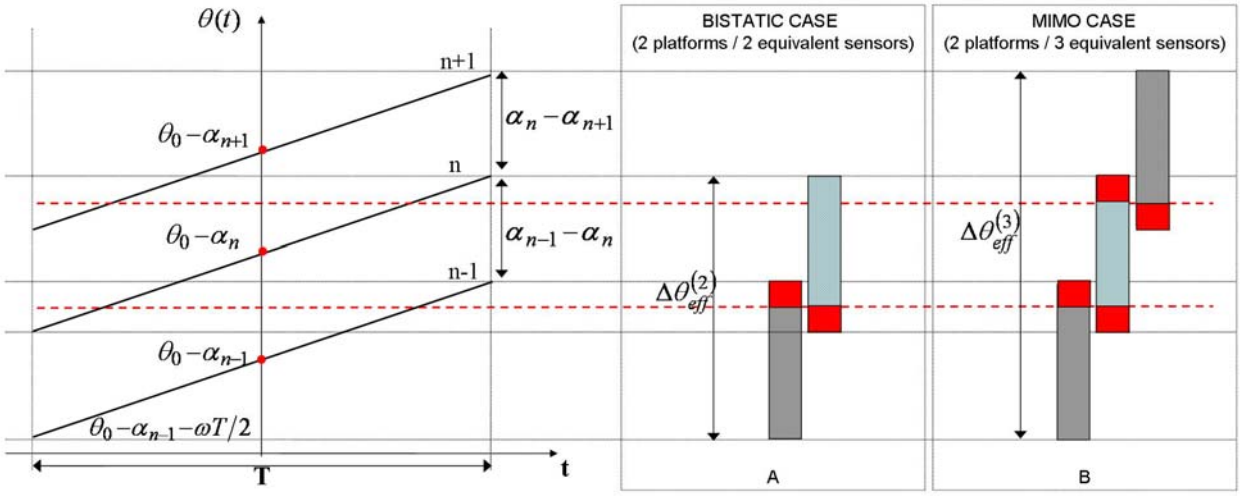

Fig. 16 – Distributed ISAR concept for enhanced cross range resolution.

The effectiveness of the proposed distributed ISAR technique is tested against a simulated point-like target at distance $r=4m$ from the scene centre, with azimuth $\theta^0=\pi/4$ and rotating with rotation rate $\omega=0.36°/\sec$. A formation of two platforms A and B is considered, carrying two X-band radar systems acquiring echoes from the scatterer for a synthetic aperture T=1.59 sec (to achieve about 1.5 m cross range resolution when a single sensor is used). The parameter α_{AB} is defined as the angular separation between the two platforms and both cases are analyzed of multistatic and MIMO distributed ISAR. For the multistatic case, platform A is supposed to carry the active radar system while platform B carries the passive device. Using the notation of the previous Sections and recalling that $\alpha_1-\alpha_2$ is the separation between the transmitting sensor 1 (on platform A) and the "fictitious" sensor 2 (corresponding to the bistatic acquisition from platform B), it yields: $\alpha_1-\alpha_2=\alpha_{AB}/2$.

In the MIMO case platform A is supposed to carry an active radar system transmitting and receiving an up-chirp while platform B is equipped with a radar system transmitting a down-chirp with two receiving channels: the first one matched to its own transmission and the second one matched to the transmission from platform A. The angular separation between the two transmitting sensors 1 (from platform A) and 3 (from platform B) is $\alpha_1-\alpha_3=\alpha_{AB}$ while the bistatic acquisition from platform B provides the fictitious sensor 2 for which $\alpha_1-\alpha_2=\alpha_{AB}/2$ applies. Fig. 17 shows the scatterer imaged in the Doppler frequency/cross range domain for conventional ISAR (a single radar sensor is used), for multistatic distributed ISAR and for MIMO distributed ISAR for different values of the angular separation α_{AB} of the two flying platforms.

In agreement with the above theory, when $\alpha_{AB}=2\omega T$ we obtain a cross-range resolution improvement γ=2 in the multistatic case: the exploitation of the data acquired from the two radar systems allows us to move from 1.5 m cross-range resolution of the conventional ISAR image to the 0.75 m of the multistatic distributed ISAR image. In the same acquisition geometry by adding a second active device and resorting to the MIMO strategy we obtain γ=3 thus achieving 0.5 m cross range resolution. When the two platforms are closer, $\alpha_{AB}=\omega T$, we have γ=1.5 for the multistatic case, thus obtaining 1 m cross-range resolution, and γ=2 in the MIMO case which provides 0.75 m cross-range resolution.

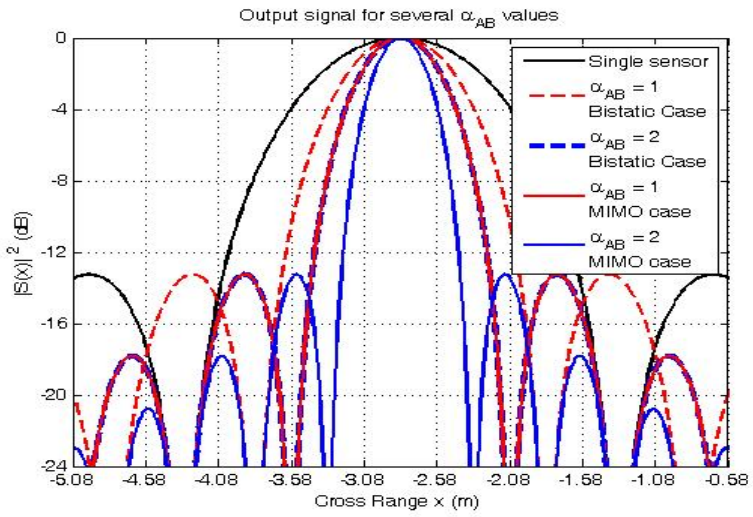

Fig. 17 – Cross range sections for single sensor and two platform distributed ISAR.

To further show the technique, the following example is shown from [4]: a distributed target is simulated consisting of a ship with about 20 scatterers, length 30 m and three different levels of superstructure; the ship rotates around the vertical axis with a rotation rate $\omega = 0.36°/\sec$. Both multistatic and MIMO distributed ISAR techniques are applied considering a formation of S=2 flying platforms.

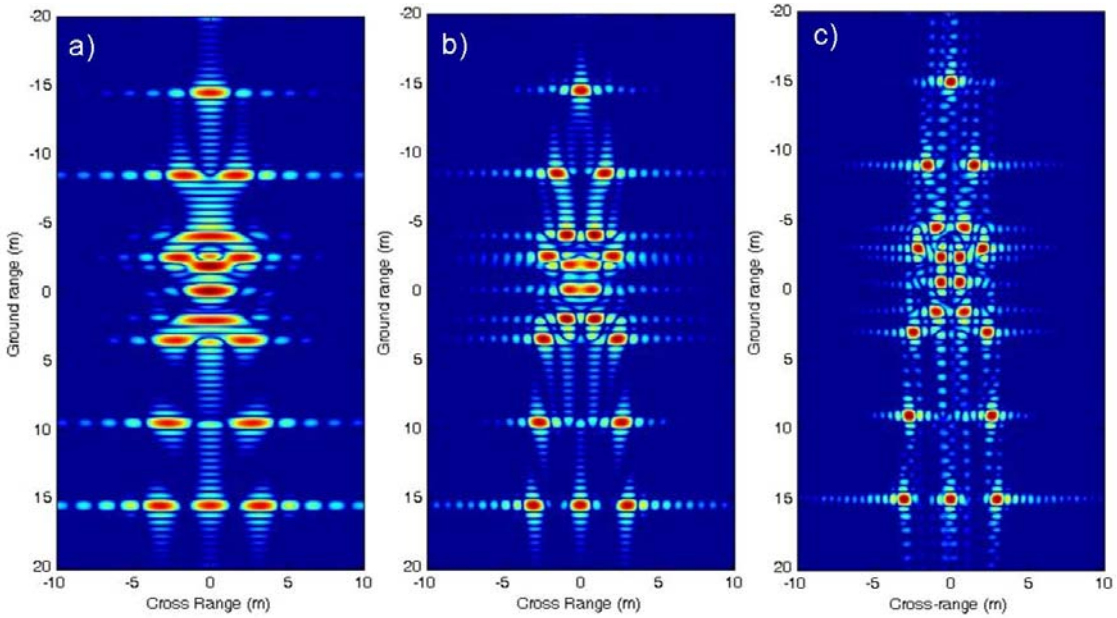

Fig. 18 – Ship conventional (cross range resolution = 1.5 m) (a), distributed – bistatic case (cross range resolution = 0.75 m) (b) and distributed – MIMO case (two platforms, three equivalent sensors, cross range resolution = 0.5 m) (c) ISAR images.

Fig. 18 and shows the images of the considered ship target obtained by using conventional and distributed ISAR technique (both multistatic and MIMO cases) with two flying platforms. Results in Fig. 18 are obtained by setting $\alpha_{AB} = 2\omega T$. In the figure the slant range resolution has been set to 50 cm using a system bandwidth of 300 MHz. A time aperture T=1.59 sec is used resulting in 1.5 m cross-range resolution when conventional ISAR is applied, Fig. 18a. For the considered acquisition geometry, the distributed ISAR technique in the multistatic case allows us to obtain a cross range resolution improvement γ=N=S; when two platforms are considered (γ=N=S=2) a cross range resolution of 0.75 m is obtained, Fig. 18b. For the same acquisition geometry the MIMO distributed ISAR strategy allows us to obtain a cross-range resolution improvement γ=N>S; in the case of two flying platforms with optimal displacement we achieve γ=N=3 and therefore obtain an image with cross range resolution of 0.5 m, Fig. 18c, instead of 1.5 m of the single sensor image, and of 0.75 m of the multistatic strategy.

3.3 Generic Distributed ISAR Concept

The extension of the dual platform case to a generic number N of sensors is straightforward, and leads to a global change of the view angle equal to:

$$\Delta\theta_{eff}^{(N)} = \theta_k^N(T/2) - \theta_k^1(-T/2) = \left[\theta_k^0 - \alpha_N + \omega T/2\right] - \left[\theta_k^0 - \alpha_1 - \omega T/2\right] = \omega T + \alpha_1 - \alpha_N \qquad \textbf{(24)}$$

The requirement for a total observation angle without gaps requires that the inequality in eq. (20) is verified for every value of *N*. This imposes an upper bound for both global observation angle and achievable cross-range resolution, corresponding to the number of equivalent sensors N:

$$\Delta\theta_{eff}^{(N)} = \Delta\theta + (N-1)\,\omega T = \Delta\theta + (N-1)\Delta\theta = N\Delta\theta \tag{25}$$

$$\Delta cr = \frac{\lambda}{2\Delta\theta_{eff}^{(N)}} = \frac{\lambda}{2(\omega T + \alpha_1 - \alpha_N)} \geq \frac{\lambda}{2N\Delta\theta} \tag{26}$$

As for the simpler case of N=2 equivalent sensors, we can obtain in principle the improvement above by building up a combined signal

$$\begin{aligned} s_{comb}(t) &= \sum_{n=1}^{N} e^{j\frac{4\pi}{\lambda}R_n} s_n(t-t_n)\,rect_{T_n}(t-t_n+\Delta t_n) = \\ &= \exp\left\{-j\frac{4\pi}{\lambda}\left[-r_k\cos\varphi_k\sin\psi_0 + r_k\sin\varphi_k\cos\psi_0\sin(\theta_k^0 + \omega t - \frac{\alpha_1+\alpha_N}{2\omega})\cos\beta_0\right]\right\} rect_{T+\frac{\alpha_1-\alpha_N}{\omega}}(t) \end{aligned} \tag{27}$$

where $t_n = \frac{\alpha_1+\alpha_N}{2\omega} - \frac{\alpha_n}{\omega}$, $T_n = \frac{\alpha_{n-1}-\alpha_{n+1}}{2\omega}$, and $\Delta t_n = \frac{\alpha_{n-1}+\alpha_{n+1}}{2\omega}$, with $\alpha_0 = \alpha_1 + \omega T$, $\alpha_{N+1} = \alpha_N - \omega T$, and constant β_n has been assumed (namely neglecting the bistatic differences). The global cross-range direction is now defined by angle $(\alpha_1+\alpha_N)/2$, so that the scatterer range and cross-range positions are respectively $x_r^k = r_k \sin\varphi_k \sin(\theta_k^0 - (\alpha_1+\alpha_N)/2)$ and $x_{cr}^k = r_k \sin\varphi_k \cos(\theta_k^0 - (\alpha_1+\alpha_N)/2)$. By comparing the analytical expressions, it is apparent that exactly the same procedure can be applied than for N=2, thus yielding a correctly positioned scatterer in cross-range with resolution $\Delta cr = \lambda/[2(\omega T + \alpha_1 - \alpha_N)\cos\beta_0]$. This shows the increased resolution corresponding to an overall angle $\omega T + \alpha_1 - \alpha_N$.

To quantify the improvement in resolution in the practical application, we define the parameter γ:

$$\gamma = \frac{\Delta\theta_{eff}^{(N)}}{\Delta\theta} = \frac{\Delta_{cr}}{\Delta_{cr}^{(N)}} \leq N \tag{28}$$

i.e. the ratio between global synthesized change of observation angle and change of observation angle of the single sensor. As apparent, this parameter has the number of equivalent sensor N as its upper bound.

In the multistatic configuration the number of equivalent sensors N is coincident with the number of real sensors S, therefore the upper bound for the improvement is given by γ≤S. With reference to the example of Fig. 16A, the increased resolution above is clearly achievable by a multistatic configuration obtained by adding more receiving-only sensors (namely N-1). The case of a TX/RX sensor plus two RX-only sensors is easily verified from the same Fig. 16A to provide a maximum improvement of the resolution of a factor γ = 3. The multistatic configuration is especially interesting for the practical application in cases

where only a single "heavy" platform is available, which can be used to carry the transmit/receive sensor (possibly even a stand-off platform), but a certain number of "light" platforms can be delivered around it (as for example unmanned aerial vehicles (UAV) or drones). In this case we show that the addition of the "light" platforms provides the increase of cross-range resolution.

Fig. 16B sketches also the basic MIMO case, where two transmit-receive platforms are used (i.e. S=2). This gives rise to a total of three equivalent sensors (i.e. N=3), the two monostatic radar (that both transmit and receive appropriate waveforms) plus the bistatic acquisition (waveform transmitted by one of the radar and received by the other one). This case is modeled by the two angles of view of the two monostatic radar sensors, α_{n-1} and α_{n+1}, and by their central angle. In this case the increase in observation angle is directly of a factor γ=N=3, which is easily obtained by setting $\alpha_{n-1} - \alpha_{n+1} = 2\omega T = 2\Delta\theta$ for the real sensors.

The MIMO configuration is especially interesting case, since it allows us to reach a greater improvement in cross range resolution than the number of available platforms. This is available because the number of equivalent sensors N is generally greater than the number of real sensors S. This is obtained by using both the monostatic acquisitions and all the bistatic acquisitions, provided that adequate orthogonal waveforms are exploited. The optimization of the positions of a set of MIMO sensors to provide maximum angular coverage without gaps has been obtained in [10]. For small number of real sensors S, Table I reports the number of effective sensors N available for a continuous aperture without gaps.

To obtain the largest possible contiguous global view angle $\Delta_{eff}^{N} = N\Delta\theta_0$, using the S sensors for our MIMO ISAR application, it is necessary to appropriately displace the real sensors. In particular, the angular displacement required between each couple of adjacent real sensors is reported in the third column of Table I, expressed in integer numbers of $\Delta\theta_0$. This derives from the direct application of the results of [10] to the MIMO ISAR case. As an example, to obtain the global effective angular spacing of $\Delta_{eff}^{N} = 9\Delta\theta_0$ for the MIMO ISAR with S=4 real sensors the angular spacings must be assigned as follows: $2\Delta\theta_0$ between sensor #1 and sensor #2, $4\Delta\theta_0$ between sensor #2 and sensor #3, $2\Delta\theta_0$ between sensor #3 and sensor #4. As apparent, the choice of the basic displacement angle $\Delta\theta_0$ is essential both to avoid the gaps in the global MIMO ISAR angle ($\Delta\theta_0 \le \omega T = \Delta\theta$), and to achieve the maximal resolution improvement (largest possible value of $\Delta\theta_0$). As apparent the optimum value is $\Delta\theta_0 = \omega T = \Delta\theta$.

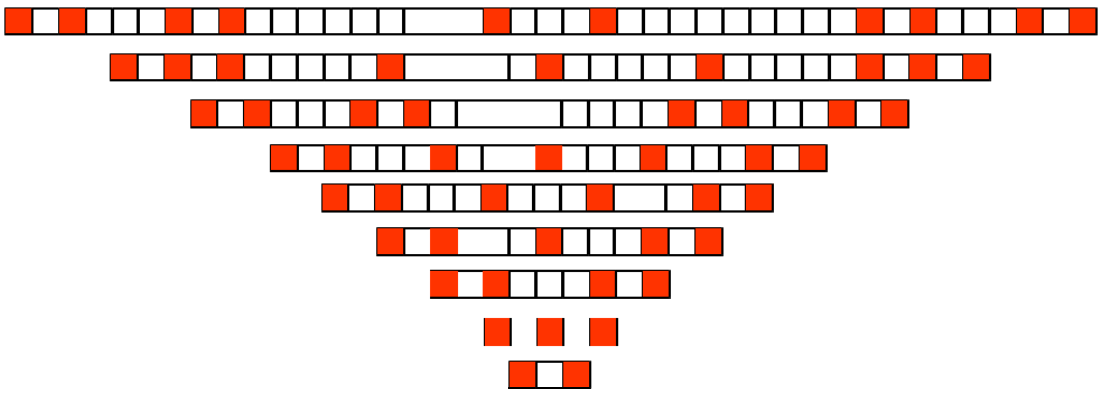

Fig. 19 – Map of real and virtual apertures (angles of view) in the MIMO distributed ISAR.

Fig. 19 shows the extension of the MIMO ISAR case to higher values of S, up to S=10, using the configurations in Table I. In particular, the red and the white squares respectively represent the real and the fictitious angular apertures used in the distributed configuration, where the term "real aperture" indicates the change of observation angle due to the target rotation observed by a real monostatic sensor, whereas "fictitious aperture" indicates the change of observation angle due to the target rotation observed by using bistatic configurations based on different transmit and receive real sensors.

In Fig. 20 the value of the maximum cross range resolution improvement is shown for both the multistatic distributed ISAR and the MIMO distributed ISAR. As it is apparent, in the multistatic case the maximum achievable cross range resolution improvement γ increases linearly with the number of platforms S since N=S. In the MIMO case the maximum γ can be considerably higher than the number of platforms S since the gain N of the MIMO configuration, that is the number of equivalent sensors considered, increases as the number of platforms increases.

The quantification of the improvement made available by the MIMO configuration with respect to the multistatic configuration is provided by the ratio N/S, that is reported in the last column of Table I. As apparent for larger values of S the improvement increases. It is interesting to consider that, the results in [10] show that in the limit for $S\rightarrow\infty$ the value of $N\rightarrow S^2$ so that the MIMO improvement tends to be quadratically related to the number of sensors and the ratio N/S goes asymptotically to S.

The focusing of a target image with improved cross-range resolution from distributed ISAR data requires an ad hoc bi-dimensional (2D) processing technique able to properly combine the radar signals acquired from the multiple sensors.

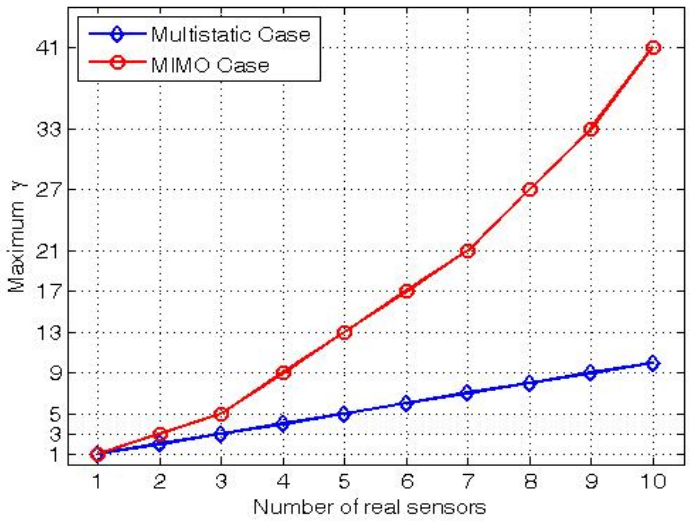

Fig. 20 – Maximum value of cross range resolution improvement γ in the multistatic and MIMO cases.

Two different approaches can be followed to obtain a full 2D distributed ISAR scheme:

(i) **Centralized Technique for Distributed ISAR focusing (CT-DISAR)**: This is the most direct implementation of the proof-of-principle scheme leads to focusing scheme, where the radar data from the N equivalent sensors must be properly pre-processed, combined coherently, and finally focused using an appropriate 2D processing scheme

(ii) **Decentralized Technique for Distributed ISAR focusing (DT-DISAR)**: This is an alternative approach that first focuses N low resolution ISAR images as collected by each single equivalent sensor, and then combines them coherently to achieve the resolution image.

Table I – Optimized MIMO configurations.

S	N	Sequence of angular spacings	N/S
2	3	2	1.5
3	5	2,2	1.6667
4	9	2,4,2	2.2500
5	13	2,4,4,2	2.6000
6	17	2,4,4,4,2	2.8333
7	21	2,4,4,4,4,2 2,2,6,6,2,2	3.0000
8	27	2,2,6,6,6,2,2 2,4,2,10,2,4,2	3.3750
9	33	2,2,6,6,6,6,2,2	3.6667
10	41	2,4,2,10,4,10,2,4,2	4.1000
11	45	2,2,2,8,8,8,8,2,2,2 2,2,6,4,8,8,4,6,2,2 2,2,6,6,6,6,6,6,2,2 2,4,2,10,4,4,10,2,4,2	4.0909
12	55	2,4,4,2,14,2,14,2,4,4,2 2,4,2,10,4,10,4,10,2,4,2	4.5833
13	65	2,4,2,10,4,10,10,4,10,2,4,2	5.0000
14	73	2,4,2,10,4,10,8,10,4,10,2,4,2	5.2143

The corresponding schemes of principle are shown respectively in Fig. 21 and Fig. 22 for the case of N equivalent sensors corresponding to S real radar systems, assuming that the 2D focusing can be approximated by a FFT. This block can be easily replaced by a full 2D ISAR focusing case, where range migration is corrected to properly focus the image.

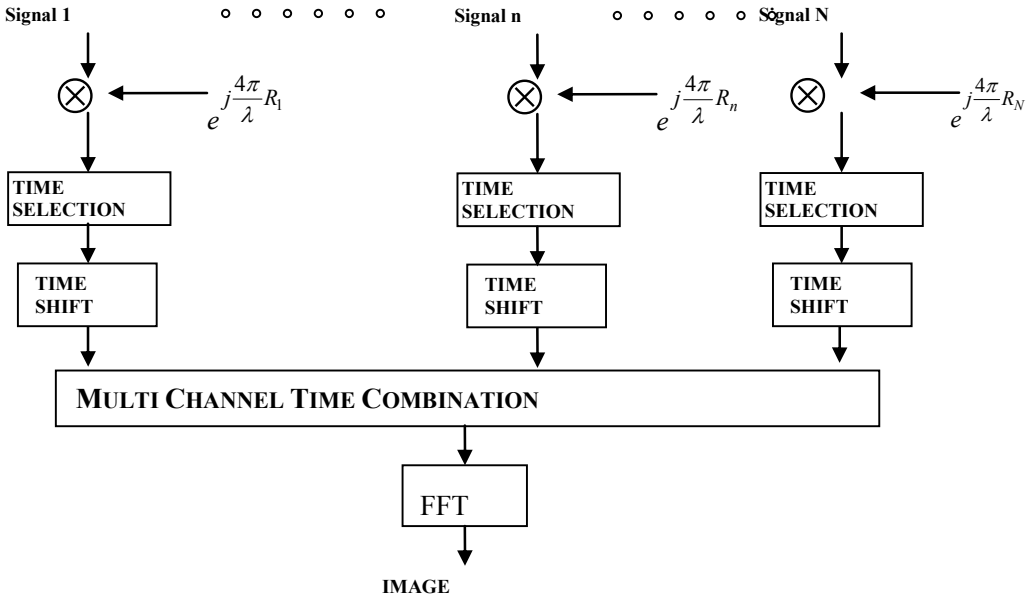

Fig. 21 - Scheme of principle for distributed ISAR with N equivalent sensors.

Fig. 23 shows the images of the considered ship target obtained by using conventional and distributed ISAR technique (both multistatic and MIMO cases) for the same case of Fig. 18 but using four flying platforms. Results in Fig. 23 are obtained by setting to $2\omega T$ the angular separation of two adjacent platforms, [4]. A time aperture T=0.53 sec is used thus providing 4.5 m cross-range resolution for the single sensor case, Fig. 23a. For the considered acquisition geometry with the four platforms we have γ=N=S=4 so that 1.125 m is obtained, Fig. 23b. For the same acquisition geometry the MIMO distributed ISAR strategy allows us to obtain a cross-range resolution improvement γ=N=9 and obtain 0.5 m cross-range resolution instead of 4.5 m of the conventional ISAR, and of 1.125 m of the multistatic strategy. The results obtained against simulated data prove the effectiveness of the proposed distributed ISAR technique.

To make the results appealing for practical application, the performance degradation has been analysed in [4], arising from errors in the knowledge of both the target rotation motion and the acquisition geometry. In this reference, experimental data collected by a ground based radar operating together with a rotating platform have also been processed by following the presented distributed ISAR technique to validate the proposed approach. Moreover, the extensions to sensors with a 2D spatial displacement, the distributed ISAR focusing with a 3D motion and the target motion estimation obtained by the distributed ISAR have been analysed respectively in [17], [18], [19].

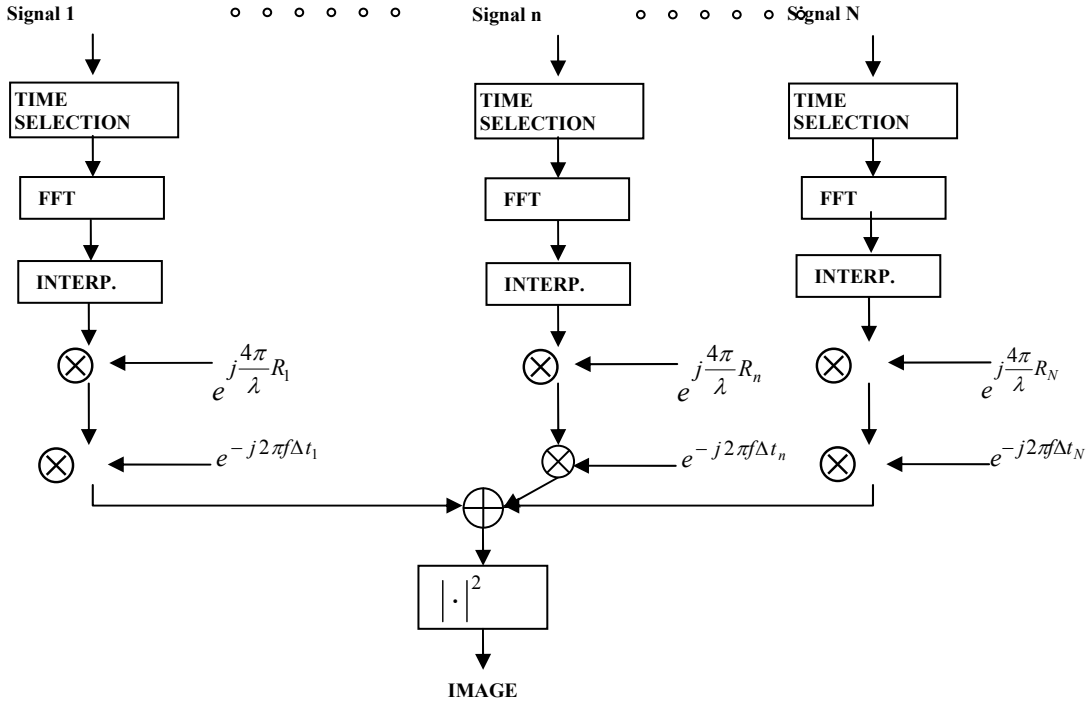

Fig. 22 - Scheme of principle for Fourier domain distributed ISAR with N equivalent sensors.

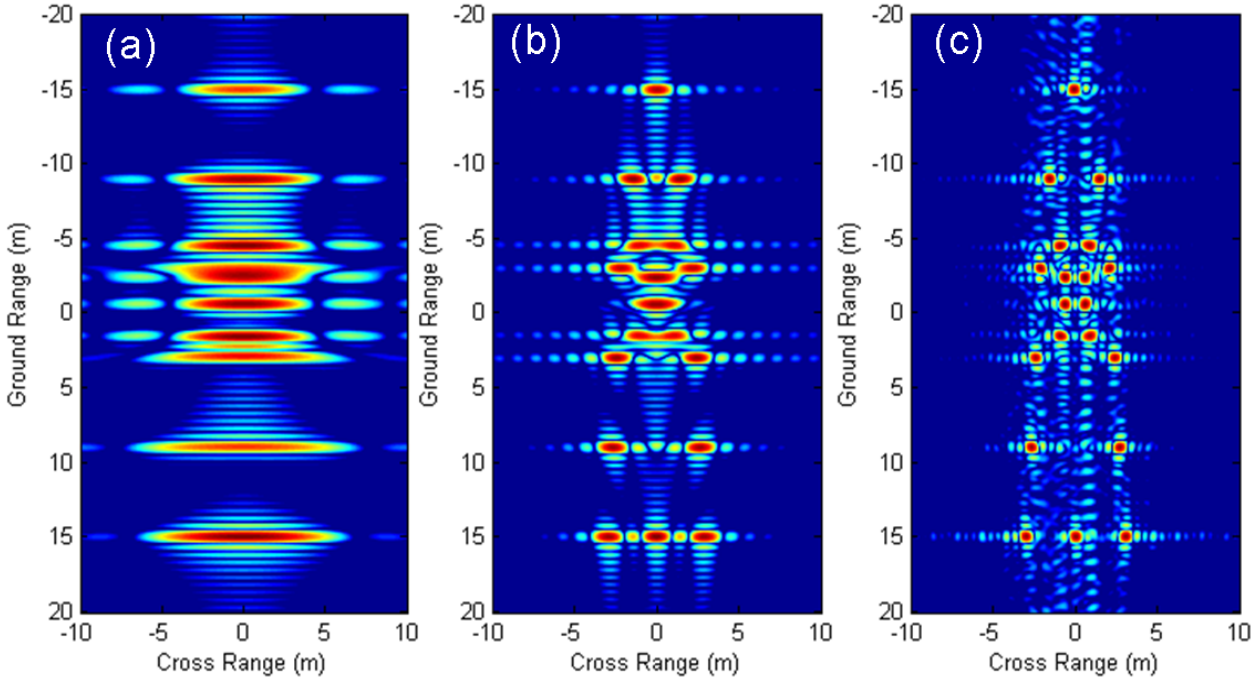

Fig. 23 – Ship conventional (cross range resolution = 4.5 m) (a), distributed –multistatic case (four platforms, cross range resolution = 1.125 m) (b) and distributed – MIMO case (four platforms, nine equivalent sensors, cross range resolution = 0.5 m) (c) ISAR images.

4.0 ACKNOWLEDGEMENTS

The author gratefully acknowledges many useful conversations with Dr. Debora Pastina, as well as the many collaborations in the research activity carried out in the latest years on this subject.

5.0 REFERENCES

[1] J.L. Walker: “Range-Doppler imaging of rotating objects”, IEEE Trans. on AES, Vol. 16, No.1, 1980, pp.23-52.

[2] D.R. Wehner, “High-Resoultion Radar”, Artech House, Boston, 1995.

[3] M.Vespe, D.Pastina, C.J.Baker, H.D.Griffiths, P.Lombardo, “Impact of angular processing technique and cross range resolution on 2D radar target classification” EUSAR 2006, Dresden (Germany), May 2006.

[4] D. Pastina, M. Bucciarelli, P. Lombardo, “Multistatic and MIMO distributed ISAR for enhanced cross-range resolution of rotating targets”, IEEE Transactions on Geoscience and Remote Sensing (GRS), Vol. 48, N. 8, August 2010, pp. 3300-3317.

[5] Raney R. K., et alii, “Precision SAR processing using chirp scaling”, IEEE Trans. GRS, 1994, 32, (4), pp. 786-799.

[6] G.Krieger, A. Moreira, "Spaceborne bi- and multistatic SAR: potential and challenges", IEE Proceedings - Radar, Sonar and Navigation, Volume 153, Issue 3, June 2006, pp. 184 – 198.

[7] G. Krieger, N. Gebert, A. Moreira, "Unambiguous SAR signal reconstruction from nonuniform displaced phase center sampling", IEEE Geoscience and Remote Sensing Letters, Volume 1, Issue 4, Oct. 2004, pp. 260 – 264.

[8] N.A. Goodman, Sih Chung Lin, D. Rajakrishna, J.M. Stiles, "Processing of multiple-receiver spaceborne arrays for wide-area SAR", IEEE Transactions on Geoscience and Remote Sensing, Volume 40, Issue 4, April 2002, pp. 841 – 852.

[9] T. Teer, N.A.Goodman, "Multistatic SAR algorithm with image combination", 2006 IEEE Conference on Radar, 24-27 April 2006.

[10] C. Correll, Jr., "Efficient Spotlight SAR MIMO Linear Collection Geometries," Proceedings of the 5th European Radar Conference, October 2008, Amsterdam.

[11] D. Cristallini D. Pastina, M. Bucciarelli, P. Lombardo, "Exploiting MIMO SAR Potentialities With Efficient Cross-Track Constellation Configurations for Improved Range Resolution", IEEE Transactions on Geoscience and Remote Sensing, Vol. 49,N. 1, January 2011, Part: 1, pp. 38- 52.

[12] Changzheng Ma; Tat Soon Yeo; Qun Zhang; Hwee Siang Tan; Jun Wang; "Three-Dimensional ISAR Imaging Based on Antenna Array", IEEE Transactions on Geoscience and Remote Sensing, Volume 46, Issue 2, Feb. 2008 Page(s):504 – 515

[13] Qun Zhang; Tat Soon Yeo; Gan Du; Shouhong Zhang; "Estimation of three-dimensional motion parameters in interferometric ISAR imaging", IEEE Transactions on Geoscience and Remote Sensing, Volume 42, Issue 2, Feb. 2004 Page(s):292 - 300

[14] D.Pastina, R.G.White, D.Coe, "A new contrast based autofocusing technique for high resolution imaging of rotating targets", EUSAR 2000, pp. 445-448.

[15] D. Pastina, "Rotation motion estimation for high resolution ISAR and hybrid SAR/ISAR target imaging", 2008 IEEE Radar Conference, Rome (Italy), May 2008.

[16] D. Pastina, C. Spina, "Slope-based frame selection and scaling technique for ship ISAR imaging", IET Proc. on Signal Proc., Vol. 2, No. 3, Sept. 2008, pp. 265-276.

[17] D. Pastina, F. Santi, M. Bucciarelli, P. Lombardo, "2D-MIMO SAR/ISAR imaging of moving targets with reconfigurable formation of platforms", 9th European Conference on Synthetic Aperture Radar, EUSAR 2012, pp. 223- 226.

[18] M. Bucciarelli, D. Pastina, "Distributed ISAR focusing for targets undergoing 3D motion", IET International Conference on Radar Systems (Radar 2012).

[19] F. Santi, M. Bucciarelli, D. Pastina, "Target rotation motion estimation from distributed ISAR data", IEEE Radar Conference, RADAR 2012, pp. 659 -664.